Coherent Change Detection Using InSAR Temporal Decorrelation Model: A Case Study for Volcanic Ash Detection

Jungkyo Jung, Duk-jin Kim, *Senior Member, IEEE*, Marco Lavalle, and Sang-Ho Yun

***Abstract*—Detection of changes caused by major events—such as earthquakes, volcanic eruptions, and floods—from interferometric synthetic aperture radar (SAR) data is challenging because of the coupled effects with temporal decorrelation caused by natural phenomena, including rain, snow, wind, and seasonal changes. The coupled effect of major events and natural phenomena sometimes leads to misinterpretation of interferometric coherence maps and often degrades the performance of change detection algorithms. To differentiate decorrelation sources caused by natural changes from those caused by an event of interest, we formulated a temporal decorrelation model that accounts for the random motion of canopy elements, temporally correlated dielectric changes, and temporally uncorrelated dielectric changes of canopy and ground. The model parameters are extracted from the interferometric pairs associated with natural changes in canopy and ground using the proposed temporal decorrelation model. In addition, the cumulative distribution functions of the temporally uncorrelated model parameters, which are associated with natural changes in canopy and ground, are estimated from interferometric pairs acquired before the event. Model parameters are also extracted from interferometric SAR data acquired across the event and compared with the cumulative probabilities of natural changes in order to calculate the probability of a major event. Subsequently, pixels with cumulative probabilities greater than 75% are marked as changed due to the event. A case study for detecting volcanic ash during the eruption of the Shinmoedake volcano in January 2011 was carried out using L-band Advanced Land Observation Satellite PALSAR data.**

***Index Terms*—Coherence change detection, synthetic aperture radar (SAR) interferometry, temporal decorrelation model, volcanic ash.**

I. Introduction

CHANGE detection using remote sensing data is a key technique for the generation of global-scale damage maps after natural hazards [1]–[3]. In the past decades, several approaches of change detection using visible and near-infrared data have been proposed [4]–[6]. These approaches, however, have not always been successful in detecting changes in the presence of canopy cover because optical sensors measure primarily the surface reflectivity. Conversely, synthetic aperture radar (SAR) microwaves can penetrate forest canopies and obtain structural information about the underlying surface, especially at longer wavelengths. In addition, remote sensing with radars has several advantages, such as independence of acquisition from cloud cover and sun illumination. These advantages are critical in many practical situations because they extend the temporal and spatial applicability of SAR-based change detection techniques.

Change detection approaches using SAR data are categorized into incoherent and coherent [7]. Incoherent change detection involves comparison of backscattering amplitude between SAR data, generally by interpreting the difference or ratio of the SAR intensity acquired before and after the event to be detected [8]–[10]. In order to enhance the changed area, log ratio and amplitude normalized differences were also introduced in [11] and [12]. In [9] and [13], incoherent change detection was performed with a filtering method in order to reduce false alarms. These efforts were further developed into unsupervised change detection techniques that automatically determine the threshold value [14], [15].

On the other hand, coherent change detection (CCD) techniques utilize the interferometric correlation estimated between interferometric pairs of SAR images [1], [16]. Analysis of cross-correlation is able to provide information about changes in scattering properties, including dielectric and structural. Many CCD techniques have produced excellent results in detecting subtle changes induced by natural hazards and human activities [7], [11], [17], [18]. These techniques were based on the statistics of the coherence [17] and difference in the coherence magnitude [16]. So far, however, the physical process that affects the statistics of the interferometric phase has not been fully considered. Coherence is affected by a variety of components. Temporal decorrelation, in particular, is a mixture of natural changes and changes possibly associated with major events. Thus, ambiguities in change detection still remain where temporal decorrelation caused by natural phenomena is dominant such as over vegetated areas, which are likely affected by wind or seasonal changes. When decorrelation caused by a certain event is coupled with temporal decorrelation from wind or rain, isolating the two different decorrelation sources is difficult and leads to poor change detection performance. Therefore, it is necessary to understand the effect of temporal

Manuscript received December 29, 2015; revised April 12, 2016; accepted April 27, 2016. Date of publication July 7, 2016; date of current version August 11, 2016. This work was supported in part by the Space Core Technology Development program through the National Research Foundation of Korea funded by the Ministry of Science, ICT and Future Planning (2011-0020884 and 2014M1A3A3A03034799) and in part by the National Aeronautics and Space Administration Applied Sciences / Disasters Program.

J. Jung and D.-J. Kim are with the School of Earth and Environmental Sciences, Seoul National University, Seoul 151-742, South Korea (e-mail: ring78@snu.ac.kr; djkim@snu.ac.kr).

M. Lavalle and S.-H. Yun are with the Jet Propulsion Laboratory, California Institute of Technology, Pasadena, CA 91109 USA (e-mail: marco.lavalle@jpl.nasa.gov; Sang-Ho.Yun@jpl.nasa.gov).

Color versions of one or more of the figures in this paper are available online at http://ieeexplore.ieee.org.

Digital Object Identifier 10.1109/TGRS.2016.2572166

decorrelation on the interferometric coherence of both natural processes and major events. To this end, in this study, we formulated a temporal decorrelation model to support interpretation of the interferometric coherence for the purpose of change detection. Modeling of temporal decorrelation was first addressed in [19] and later extended in [20] and [21] to polarimetric SAR interferometry.

In this paper, we focus on detecting the deposit of volcanic ash after an eruption through application of a temporal decorrelation model and a multitemporal SAR dataset on diverse surface types. The main idea of the proposed technique is to identify the areas where the loss of coherence is more significant than the expected amount of decorrelation due to motion of vegetation elements and dielectric changes in vegetation and ground, which can be predicted from the proposed temporal decorrelation model. The remainder of this paper is organized as follows. In Section II, we review the interferometric decorrelation sources and propose a temporal decorrelation model to interpret coherence observations from multitemporal and single-polarization SAR data. In Section III, we describe and illustrate how to apply the temporal decorrelation model and extract its parameters using Japan Aerospace Exploration Agency's (JAXA's) Advanced Land Observation Satellite (ALOS) PALSAR data acquired before and after the eruption of the Shinmoedake volcano in Japan in 2011. Using *in situ* data, we also validate and discuss the limitations of our approach. In Section IV, we summarize the study, discuss potential issues, and suggest possible methods to achieve more accurate results.

II. Underlying Theory

In this section, we review the decorrelation components of the interferometric coherence and introduce the temporal decorrelation model that will be used in Section III. Because our main objective is the modeling of temporal decorrelation and interpretation of the observed coherence for change detection, we describe the other decorrelation components only briefly. In addition, the dataset available in this study was acquired by ALOS-PALSAR, which has a temporal baseline of months or years. Thus, we formulated the temporal decorrelation model so that it is able to interpret the coherence from long temporal interferometric pairs.

A. Interferometric Coherence Sources

It is necessary to consider the basic properties of coherence and decorrelation before designing the temporal decorrelation model. The normalized complex correlation coefficient or complex coherence is estimated as [22], [23]

$$\gamma = \frac{\langle s_1\, s_2^* \rangle}{\sqrt{\langle s_1\, s_1^* \rangle \langle s_2\, s_2^* \rangle}} \tag{1}$$

where s_1 and s_2 are the complex pixel values of two SAR images and the angular brackets denote ensemble averaging. The magnitude of the complex correlation coefficient is often called simply "coherence" and is indicated hereafter by γ. In general, the coherence ranges between 0 and 1. For completely coherent scatterers, $\gamma = 1$; however, this condition is extremely uncommon in repeat-pass interferometry owing to a variety of decorrelation effects. Decorrelation can be divided into four components: geometric, volumetric, temporal, and thermal decorrelation [22]–[24]

$$\gamma = \gamma_{\text{geometric}} \gamma_{\text{thermal}} \gamma_{\text{temporal\&volume}}. \tag{2}$$

In single-pass interferometry, where two or more images are acquired simultaneously, there are no effects related to changes in scattering characteristics such as motion of the scatterers and biological growth; thus, temporal decorrelation is negligible. However, in repeat-pass interferometry, where images are acquired at different times and look angles, temporal and volumetric decorrelation sources, as well as thermal and geometric decorrelation sources, affect the total coherence. In addition, volumetric and temporal decorrelation sources are coupled in vegetated areas and are difficult to separate [21].

Thermal decorrelation is determined by thermal noise in the interferometric instrument. Thermal noise is typically assumed to have circular-Gaussian statistics. Thermal decorrelation is related to the signal-to-noise ratio (SNR) of the scatterers illuminated by radar signal [22], [23]

$$\gamma_{\text{thermal}} = \frac{1}{1 + \text{SNR}^{-1}}. \tag{3}$$

The variance of the interferometric phase depends on the SNR. Thus, pixels with high SNR generally exhibit high coherence [24]. Because the magnitude of the returned SAR signal varies depending on the response of the scatterers, the thermal decorrelation also varies pixel by pixel. The SNR can be estimated by dividing the radar backscattering coefficient (σ^0) by the noise equivalent sigma zero (NESZ) [25].

Spatial decorrelation (also known as "baseline decorrelation") occurs when sensor positions are different during acquisitions and comprises two components: geometric decorrelation (or "surface" decorrelation) and volumetric decorrelation [22], [23], [26]. Geometric decorrelation can be compensated by common-wavenumber spectral filtering [23].

Volumetric decorrelation originates from the scattering of radar microwaves within a volume [22], [26] such as forest canopies. Recent research efforts using polarimetric SAR interferometry aim at retrieving the structural parameters of forests using a two-layer model in which the properties of coherence and interferometric phase are sensitive to forest vertical structure and height. In the random-volume-over-ground (RVoG) model proposed in [27] and [28], volumetric decorrelation is defined as a function of several parameters including forest height h_V, extinction coefficient κ_e, ground-to-volume ratio μ, and vertical wavenumber k_z. In the RVoG model, κ_e is a function of the scatterers' density in the volume. In [28], temporal decorrelation was omitted because the data were acquired over a short time period (specifically, a few minutes). Under the assumption of no temporal decorrelation, the RVoG model is able to interpret the volumetric decorrelation in polarimetric SAR interferometry. The coherence determined from ground

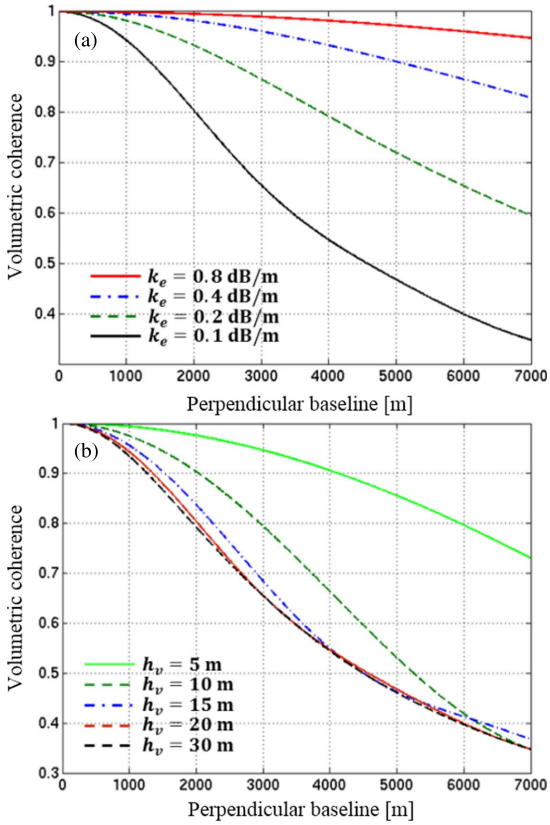

Fig. 1. Coherence predicted by the RVoG model for a variety of forests parameters using the ALOS-PALSAR geometry. (a) As a function of wavenumber and extinction coefficient k_e assuming canopy height $h_V = 20$ m. (b) As a function of wavenumber and canopy height assuming vertical extinction 0.1 dB/m.

and volume γ_{vg} and the volumetric coherence of the canopy γ_v are expressed as

$$\gamma_{vg} = \frac{\gamma_v + \mu}{1 + \mu} \tag{4}$$

$$\gamma_v = \frac{\int_0^{h_V} \exp[\rho(z)] \exp(ik_z z) dz}{\int_0^{h_V} \exp[\rho(z)] dz} \tag{5}$$

$$k_z = \frac{4\pi\Delta\theta}{\lambda \sin\theta_0} \text{ and } \rho(z) = \frac{2\kappa_e z}{\cos\theta} \tag{6}$$

where θ_0 is the incidence angle, γ is the radar wavelength, and $\Delta\theta$ is the difference in look angle due to the baseline B. Estimation of the model parameters from the volumetric coherence is possible using polarimetric interferometric SAR data or multibaseline data [28]–[30]. However, in the general case of repeat-pass interferometry using single-polarimetric SAR data, use of the RVoG model is restricted because temporal decorrelation strongly affects the coherence and is coupled with the volumetric decorrelation.

Several assumptions can be incorporated into the RVoG model, depending on the properties of the forest and the characteristics of the interferometer. In this paper, we bound the volumetric decorrelation observed by ALOS-PALSAR to minimal value so that the observed total coherence is dominated by temporal decorrelation, which is key to estimating the changes in the imaged scenes. We plotted the RVoG coherence versus the perpendicular baseline for different values of canopy extinction coefficient and canopy height in Fig. 1. The figure shows that the volumetric coherence is higher than 0.94 for perpendicular baselines smaller than 1 km assuming 20-m canopy height and 0.1-dB/m extinction coefficient. Therefore, in order to neglect the contribution of the volumetric decorrelation in the total observed coherence, the use of an interferometric baseline shorter than 1 km (i.e., an interferometric wavenumber smaller than 0.10 rad/m) is recommended. Clearly, this choice reduces the number of interferometric pairs that can be effectively processed for change detection. Therefore, proper selection of baseline in accordance with the properties of the canopy and the characteristics of interferometer, along with a sufficient quantity of usable dataset, are key considerations in this study.

B. Temporal Decorrelation Model

Temporal decorrelation is associated with changes in the dielectric and structural properties of the scatterers [22], [31]. These changes are more likely to occur over longer interferometric time intervals, which are typical of a spaceborne interferometer. Among the various land covers, vegetated areas are more affected by temporal decorrelation owing to the motion of leaves and dielectric changes associated with natural growth and leaves falling. All of these effects change the complex reflectivity in the radar resolution cell and cause decorrelation in interferometric radar signals.

In this paper, we formulate a temporal decorrelation model to describe the coherence behavior of spaceborne interferometric acquisitions with temporal baseline on the order of months or years. Temporal decorrelation is decomposed into several terms depending on where the temporal decorrelation occurs, i.e., volume or ground, and what induces the temporal decorrelation, i.e., motion or dielectric changes. Motion-induced temporal decorrelation occurs when the scatterers change their positions during the time between the acquisitions of two interferometric images [22]. Leaves and branches are likely to be randomly rearranged by the wind, and their positions are uncorrelated with the initial positions. Thus, the motion in the canopy occurs within timescales of seconds. The random motion over ground (RMoG) model presented in [20] and [21] provides a model for the coherence associated with the random motion. In the particular case of zero baseline length (i.e., $k_z = 0$), the RMoG model can be written as

$$\gamma_t = \frac{\gamma_m^v + \mu}{1 + \mu} \tag{7}$$

In (7), we have assumed zero temporal decorrelation at the ground level, where

$$\gamma_m^v = \frac{\int_0^{h_V} \exp\left[-\frac{1}{2}\left(\frac{4\pi}{\lambda}\right)^2 \sigma_r^2(z)\right] \exp[\rho(z)] dz}{\int_0^{h_V} \exp[\rho(z)] dz}. \tag{8}$$

γ_m^v is the temporal decorrelation of the canopy layer, $\rho(z)$ is the extinction profile in the volume, z is the height from the ground in vertical direction, μ is the ground-to-volume ratio, and $\sigma_r(z)$ is the function that describes the motion standard deviation. Here we assume that the standard deviation of the random motion $\sigma_r(z)$ changes linearly with the vertical location and is zero at the ground level, i.e., $\sigma_r(z) = z\sigma_r/h_r$. Then (8) becomes

$$\gamma_m^v = \frac{\int_0^{h_V} \exp\left[-\frac{1}{2}\left(\frac{4\pi\sigma_r}{\lambda\, h_r} z\right)^2\right] \exp[\rho(z)] dz}{\int_0^{h_V} \exp[\rho(z)] dz} \tag{9}$$

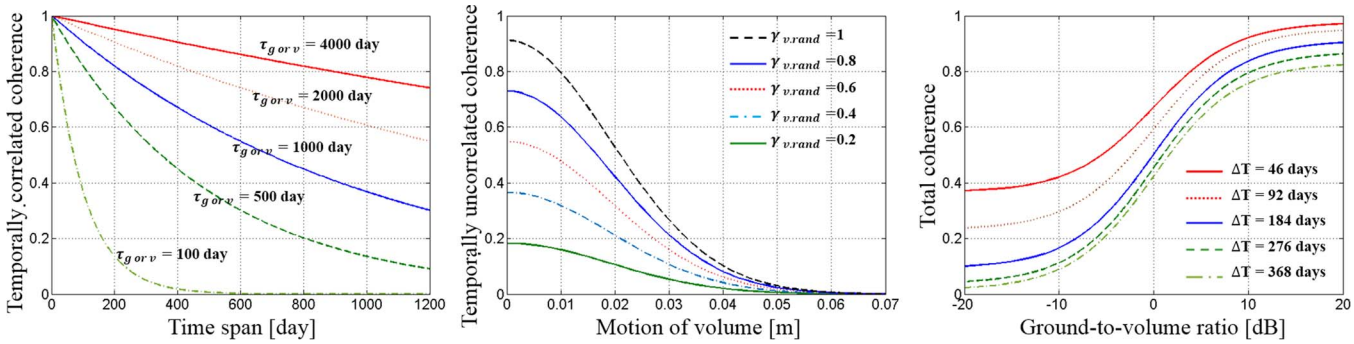

Fig. 2. (a) Temporally correlated coherence $\gamma_{d,\text{time}}$ against interferometric timespan. (b) Temporally uncorrelated coherence γ^v_{rand} induced by motion σ^{ξ}_r and random dielectric changes $\gamma^v_{d,\text{rand}}$. (c) Total coherence changes versus ground-to-volume ratio assuming $\tau_g = 2\,000$ days, $\tau_v = 100$ days, $\sigma_\xi = 2$ cm, and no temporally uncorrelated dielectric changes.

where the motion is standard deviation σ_r at reference height h_r. According to the mean value theorem for definite integrals, given a definite integral of the form $\int_a^b f(x)g(x)dx$, where f and g are continuous in the interval (a, b), we can find a mean value "c" of $f(x)$ on $[a, b]$ such that $\int_a^b f(x)g(x)dx = f(c)\int_a^b g(x)dx$. The theorem can be applied to (9), in which case γ^v_m becomes

$$\gamma^v_m = \exp\left[-\frac{1}{2}\left(\frac{4\pi}{\lambda}\sigma_\xi\right)^2\right] \tag{10}$$

where

$$\sigma_\xi = \frac{\sigma_r}{h_r}\xi. \tag{11}$$

σ_ξ is the motion standard deviation in the volume, and ξ is an *intermediate height*, which ranges between zero and h_V. This algebraic manipulation has the advantage of reducing the number of model parameters from three (h_V, σ_r, and κ_e) to one (σ_ξ) because extraction of tree height and extinction is out of the scope of this paper.

Natural phenomena such as rain, snow, falling leaves, and weather change not only the backscattering amplitude of the scatterers but also the scattering phase, which results in temporal decorrelation. Therefore, additional terms are required to properly model the temporal decorrelation in the presence of dielectric changes. Here, we add γ^v_d and γ^g_d to account for dielectric changes in volume and ground, respectively. γ^v_d and γ^g_d can be divided into two terms, respectively, the decorrelation associated with temporally correlated dielectric changes, $\gamma^v_{d,\text{time}}$ and $\gamma^g_{d,\text{time}}$, and the decorrelation associated with temporally uncorrelated dielectric changes, $\gamma^v_{d,\text{rand}}$ and $\gamma^g_{d,\text{rand}}$. The temporally correlated terms describe the temporal changes of the scattering properties; hence, the coherence decreases as the temporal baseline between two SAR acquisitions increases. Several studies assume an exponential model to quantify the temporally correlated coherence changes [19], [32]. The temporally correlated coherence can be expressed as

$$\gamma_{d,\text{time}} = \exp\left(-\frac{\Delta T}{\tau}\right) \tag{12}$$

where τ is the characteristic time (measured in days), over which coherence decreases by a factor of e, and ΔT is the time span of two SAR acquisitions. $\gamma_{d,\text{time}}$ assumes that the change rate τ is constant over time. This phenomenon has already been explained in the literature using Brownian motion and a Markovian model [19], [32]. However, it is worth noting that the difference between our model and the models in [19] and [32] is that we apply the temporally correlated dielectric change to both ground and volume. We plotted the temporally correlated changes $\gamma^v_{d,\text{time}}$ and $\gamma^g_{d,\text{time}}$ versus time in Fig. 2(a). The terms $\gamma^v_{d,\text{time}}$ and $\gamma^g_{d,\text{time}}$ are more stable with time for large values of τ than for smaller values of τ.

Furthermore, the temporally uncorrelated dielectric changes $\gamma_{d,\text{rand}}$ explain the randomly generated decorrelation such as rain, snow, and collapse of man-made structures. Decorrelation caused by sudden events has been reported in the literature [11], [17], and these phenomena were often observed in coherence maps. We can usually observe different coherence values in the same time intervals over the same scatterers. According to the proposed model, these coherent differences are interpreted as an effect of the temporally uncorrelated dielectric change. The temporally uncorrelated term $\gamma_{d,\text{rand}}$ can be divided into $\gamma^g_{d,\text{rand}}$ and $\gamma^v_{d,\text{rand}}$ depending on where decorrelation happens.

Therefore, the decorrelation caused by dielectric changes in volume and ground can be expressed as follows:

$$\begin{aligned}\gamma^v_d &= \gamma^v_{d,\text{time}}\gamma^v_{d,\text{rand}} = \exp\left[-\frac{\Delta T}{\tau_v}\right]\gamma^v_{d,\text{rand}} \\ \gamma^g_d &= \gamma^g_{d,\text{time}}\gamma^g_{d,\text{rand}} = \exp\left[-\frac{\Delta T}{\tau_g}\right]\gamma^g_{d,\text{rand}}.\end{aligned} \tag{13}$$

From (7) to (13), the temporal decorrelation observed in multitemporal coherence maps can be written as

$$\gamma_t = \frac{1}{1+\mu}\exp\left(-\frac{\Delta T}{\tau_v}\right)\gamma^v_{\text{rand}} + \frac{\mu}{1+\mu}\exp\left(\frac{\Delta T}{\tau_g}\right)\gamma^g_{d,\text{rand}} \tag{14}$$

where

$$\gamma^v_{\text{rand}} = \exp\left[-\frac{1}{2}\left(\frac{4\pi}{\lambda}\sigma_\xi\right)^2\right]\gamma^v_{d,\text{rand}}. \tag{15}$$

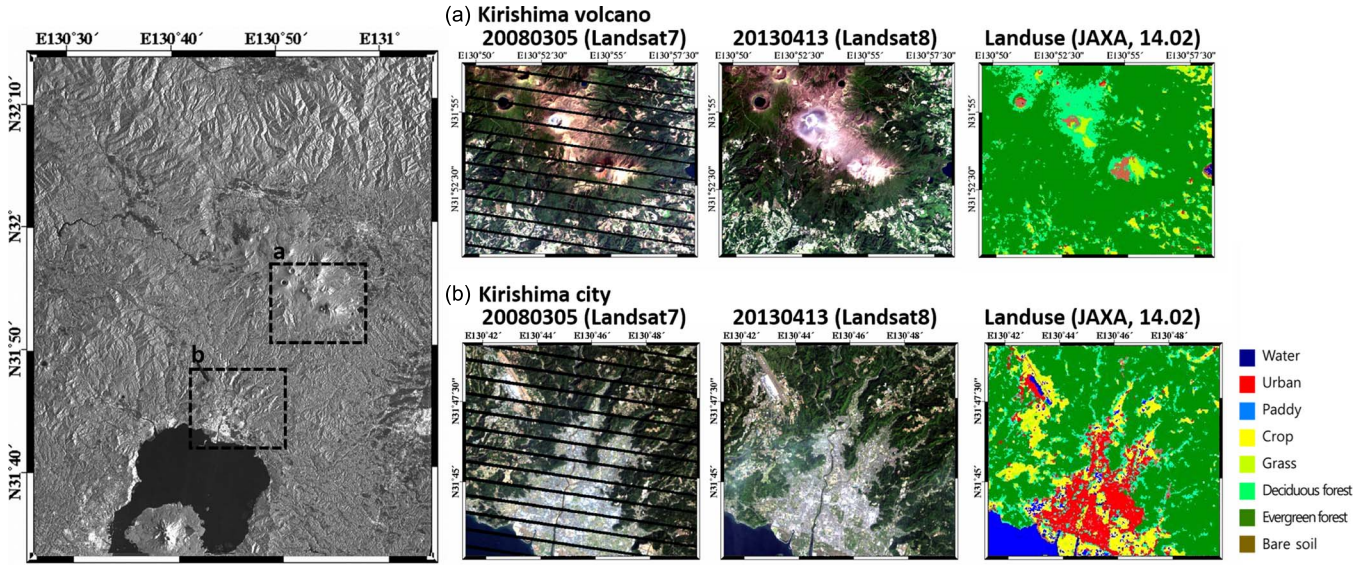

Fig. 3. Study area in Kyushu, Japan. (Left) SAR amplitude image and the rectangular boxes are the Kirishima volcano cluster and Kirishima city, respectively. (Right) Landsat images acquired on March 5, 2008, and April 13, 2013. Land-use maps provided by JAXA are also presented in the figure.

Note that the temporally uncorrelated dielectric change $\gamma^v_{d,\mathrm{rand}}$ and motion σ_ξ in volume have similarities in temporal behavior, which decrease the coherence randomly over time. The interesting point is that, if the dielectric change is high ($\gamma^v_{d,\mathrm{rand}}$ is low) in volume, the effect of motion is less than in the case where dielectric changes are low ($\gamma^v_{d,\mathrm{rand}}$ is high), as shown in Fig. 2(b). In this paper, the individual extraction of two terms is unnecessary; consequently, we can merge them as temporally uncorrelated changes γ^v_{rand}.

According to the proposed model, the total temporal coherence γ_t is dependent on the ground-to-volume ratio μ, as shown in Fig. 2(c). The fact that the coherence differences depend on μ implies that coherence could vary depending on the land cover, the properties of the forest canopy, and the proportion of dominant scattering. It is also worth noting that the formulated temporal decorrelation model can interpret the coherence map generated from an interferometric pair with timescales of years. However, if the interferometric pair is acquired within a few seconds, $\Delta T \sim 0$, (14) becomes the RMoG model with the assumption of no ground motion as in (7).

III. Change Detection Case Study

A. Study Area and Coherence Map Generation

In order to validate the temporal decorrelation model and detect changed areas, we chose the Shinmoedake volcano in the Kirishima volcano cluster and Kirishima city as study areas. The Shinmoedake volcano is one of the most active volcanoes in Japan, and its last eruption was in January 2011. A thick layer of volcanic ash was deposited on the southeastern part of the volcano [33]. According to the land-use map (ver. 2014.04) provided by JAXA [34], the peak and the area around the rim of the Shinmoedake volcano mainly consist of bare soil. The Kirishima volcano cluster is surrounded by evergreen and deciduous forest as shown in Fig. 3. Thus, the volcanic ash emitted in 2011 mainly fell on bare soil and vegetated areas. As stated in Section II, the decorrelation caused by the volcanic eruption event may appear on top of the temporal decorrelation caused by the natural background change. Such temporal decorrelation caused by natural change may be misinterpreted as the contribution of the major event. In particular, this misinterpretation might be severe in forests because vegetated areas are prone to temporal decorrelation. Therefore, understanding and predicting the coherence behavior using a temporal decorrelation model are essential for accurate interpretation of coherence. Kirishima city was chosen for comparison of change detection results in order to evaluate the performance of our change detection method.

In this paper, we used 21 ALOS-PALSAR datasets with HH polarization of the study area acquired from January 2007 to April 2011 (about 4.2 years) in descending orbit at a 38° incidence angle. The interferometric pairs were separated into pre-eruption and coeruption pairs. Only two images were acquired after the volcanic eruption in January 2011 (March 5, 2011, and April 20, 2011). We assigned the coherence maps generated using pre-eruption data as the reference pairs, and these coherence maps were used to interpret the temporal behaviors of natural phenomena via a temporal decorrelation model. The coherence maps generated using coeruption data were assigned to the event pairs. Interferometric coherence estimation was performed after 32 multilooking, common band filtering, and removal of flat-earth and the topographic phase. Thus, the bias of coherence and geometrical decorrelation were assumed to be negligible. The SNRs were estimated by dividing sigma zero (σ°) by NESZ [25]. The minimum NESZ was approximately -23 dB in HH polarization of FBS and FBD modes [35]. The acquired dataset showed a high SNR for the forest and urban areas, specifically > 9, and a low SNR in the sea area, specifically < 5. The thermal decorrelation of the forest and urban areas was less than 0.13; thus, thermal noise may not have been the cause of the major decorrelation in those areas. However, the areas with a low SNR, such as the sea and rivers, are prone to thermal decorrelation. Therefore, areas consisting of sea were masked out, and the analysis was mainly performed on bare soil, urban area, and forest, which have high SNR.

B. Extraction of Temporal Decorrelation Parameters

If we have N interferometric pairs (sum of the number of reference and event pairs), the number of model parameters becomes $2N+3$ in multitemporal and single-polarization interferometer because $\gamma^v_{\mathrm{rand}}\ (N)$ and $\gamma^g_{d,\mathrm{rand}}\ (N)$ are pair-variant variables and μ, τ_g, and τ_v are pair-invariant variables. Consequently, extracting the model parameters is a challenging task. Despite the analytic limitation, it is possible to estimate the model parameters of the proposed temporal decorrelation model under several realistic assumptions as described hereafter.

In the first step, the highest coherence values were identified in each time interval in the reference pairs. We identified an exponential curve envelope defined by the highest coherence values. The highest coherence values indicate that the coherence is most likely unaffected by temporally uncorrelated temporal decorrelation, which means that σ^{ξ}_r is almost zero, and $\gamma^v_{d,\mathrm{rand}}$ and $\gamma^g_{d,\mathrm{rand}}$ are almost equal to one. This assumption is beneficial to simplification of (14) to

$$\gamma_t^{\mathrm{high}} = \frac{1}{1+\mu}\exp\left(-\frac{\Delta T}{\tau_v}\right) + \frac{\mu}{1+\mu}\exp\left(-\frac{\Delta T}{\tau_g}\right). \quad (16)$$

The second step is to estimate the ground-to-volume ratio μ and the characteristic time in the ground τ_g and in the volume τ_v in (16). This procedure was performed using curve fitting to the highest points. The curve fitting was applied so that the fitted curve was closest and higher than the selected highest coherences, as shown in Fig. 4. In addition, the model parameters τ_v, τ_g, and μ all should be greater than zero so that they reflect realistic conditions. The highest points are used for curve fitting because any changes in their structural and dielectric properties would result only in decorrelation. Furthermore, corresponding model parameters γ^v_{rand} and $\gamma^g_{d,\mathrm{rand}}$ are constrained in the range zero to one. If the coherence points are located over the envelope, the model parameters are out of the range, and the possible explanation about the physical meaning does not exist.

The accuracy of estimation using maxima is deeply related to the number of available pairs and time intervals. Because (16) assumes no γ^v_{rand} and $\gamma^g_{d,\mathrm{rand}}$, this assumption can be successful when there are sufficient numbers of scenes and pairs. Furthermore, the number of maxima is important because the shape of the envelope is determined by maxima values. Therefore, long temporal baseline or many time intervals are also keys to more accurate estimation. In our study, although we generated coherence maps with baseline within 5000 m, most cases showed that coherences within 1000 m are closer to the envelope. In addition, the model parameters extracted from coherence showed high correlation with those with 1000 m. Therefore, we can state that, on the basis of the coherences with baseline within 1000 m tending to be representative of all coherence maps, sufficient pairs and time intervals (or temporal baseline) were included in our analysis.

As shown in Fig. 5 and Table I, the extracted parameters have different characteristic time and ground-to volume ratios depending on the surface type. A high μ means that coherence is determined by one dominant scattering (ground), and τ_v is not important in the analysis. The high μ value is mainly observed in the bare soil and the man-made structures (areas A and B in Fig. 5). The τ_g value is higher in the man-made structures than in the bare soil because they are less affected by natural changes. Furthermore, an interesting observation is that the values of μ, τ_g, and τ_v are different even in the same surface type, i.e., evergreen forest denoted as C and D in Fig. 6. Because the ground-to-volume ratio is related to not only the surface type but also the properties of the canopy, a vegetated area could have a high μ value if the forest is not dense.

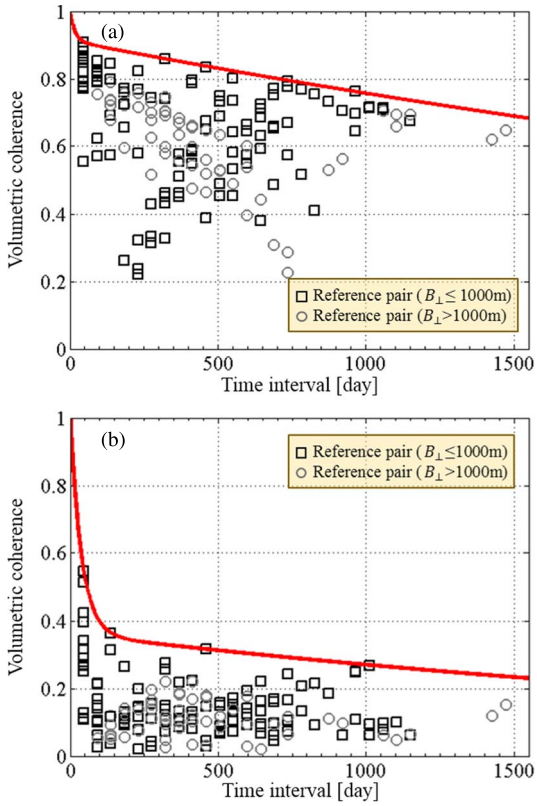

Fig. 4. Temporal coherence in (a) man-made structure (denoted B in Fig. 6) and in (b) forest area (denoted D in Fig. 6). Squares and circles are the measured coherences. Red lines indicate decorrelation related to temporally correlated dielectric changes.

The third step is the calculation of the portion (or contribution) of coherence between ground $\alpha_g = \gamma^g_{d,\mathrm{time}}/(\gamma^g_{d,\mathrm{time}} + \gamma^v_{d,\mathrm{time}})$ and volume $\alpha_v = 1-\alpha_g$ in each time interval, based on the estimated μ, τ_g, and τ_v. Even though we already extracted the parameters τ_g, τ_v, and μ in preceding step two, the number of unknown variables is $2N$, which exceeds the number of coherence maps N. Therefore, we need to apply another assumption to reduce the number of variables. In our study, α_g is a key factor in solving the problem. Portion α_g is a timespan-variant variable. In the general case, α_g increases in temporally correlated coherence as the timespan increases because τ_g is higher than τ_v. The targets such as man-made structures and bare soil have high μ; thus, the ground contribution is assumed to be dominant in every timespan.

The fourth step is the estimation of the random dielectric changes of ground $\gamma^g_{d,\mathrm{rand}}$. In the pixels with a high proportion of the ground component, the temporal decorrelation is

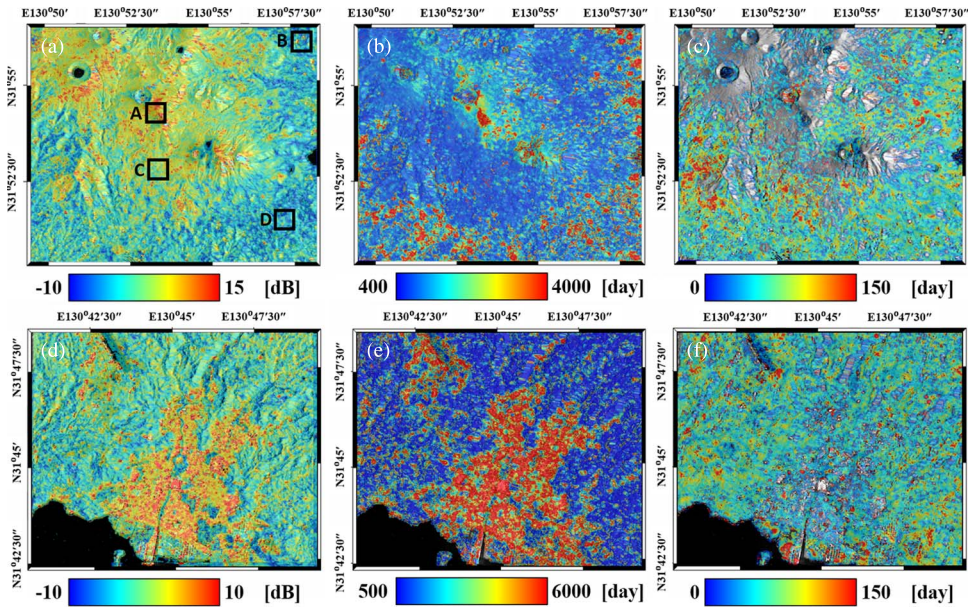

Fig. 5. (a) and (d) Estimated ground-to-volume ratio μ, (b) and (e) characteristic time τ_g, and (c) and (f) characteristic time of volume τ_v. In (a), A, B, and C and D correspond to bare soil, man-made structure, and evergreen forest, respectively.

TABLE I
EXTRACTED PARAMETERS OF THE LABELED AREAS IN FIG. 5

Label	Landuse	Ground to volume ratio	Characteristic time [days]		Dominant scattering	Days when coherence is 0.5	Coherence after revisit intervals		
		μ	τ_g (ground)	τ_v (volume)			46 days	92 days	138 days
A	Bare soil	9.43	2888	77	Ground scattering dominant	1711	0.94	0.90	0.88
B	Man-made structure	9.89	6313	53	Ground scattering dominant	3768	0.94	0.91	0.90
C	Evergreen forest	4.05	627	142	Coupled scattering (Ground > Volume)	322	0.89	0.80	0.72
D	Evergreen forest	0.53	1219	49	Coupled scattering (Volume > Ground)	65	0.59	0.42	0.35

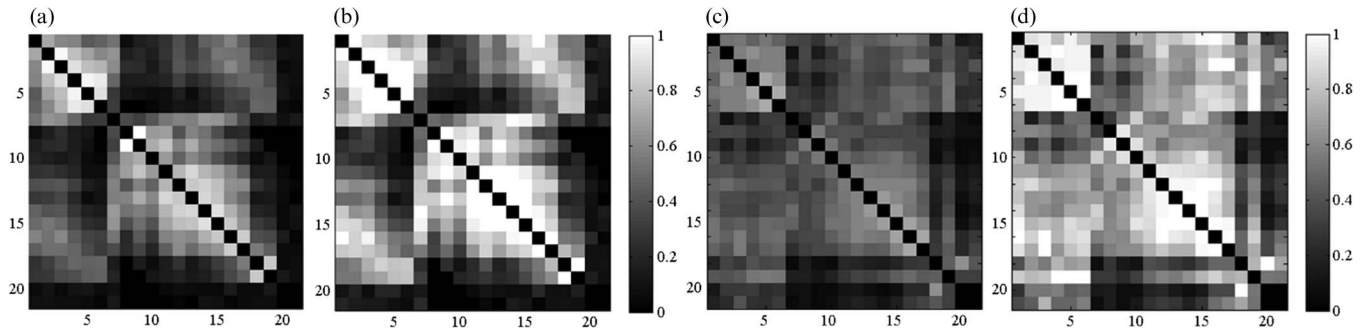

Fig. 6. (a and c) Two examples of coherence and (b and d) $\gamma^g_{d,\mathrm{rand}}$ matrices. (a) and (b) show the temporal behavior of bare soil, denoted A in Fig. 5, and (c) and (d) are denoted B in Fig. 5.

determined by only ground-dominant scattering, i.e., (16) is reformulated as

$$\text{if } \alpha_g > 0.9,\ \gamma_t^{\mathrm{high}} = \exp\left(-\frac{\Delta T}{\tau_g}\right) \tag{17}$$

$$\gamma^g_{d,\mathrm{rand}} = \frac{\gamma_{\mathrm{obs}}}{\left[\exp\left(-\frac{\Delta T}{\tau_g}\right)\right]}. \tag{18}$$

Thus, it is necessary to find ground-scattering dominant pixels before performing (18). The decorrelation components $\gamma^g_{d,\mathrm{rand}}$ are related to the changes in the dielectric properties induced by rain, snow, and seasonal changes. Therefore, the extracted parameters $\gamma^g_{d,\mathrm{rand}}$ can be used to explain loss of coherence and statistical analysis of natural phenomena on ground-scattering dominant pixels. It is worth noting that pixels with high α_g and μ are usually less affected by the contribution of the volume. This implies that the perpendicular baseline criterion is unnecessary and that pairs with higher baseline are available for extracting $\gamma^g_{d,\mathrm{rand}}$.

The fifth step is the extraction of the model parameters $\gamma^g_{d,\mathrm{rand}}$ and γ^v_{rand} in the pixels where the effects are coupled ($\alpha_g \leq 0.9$). According to the model (14), each decorrelation caused by the temporally uncorrelated changes starts from each coherence level of the temporally correlated changes. Thus, the logical implication that "if one of the temporally correlated changes is dominant, then the corresponding temporally uncorrelated changes is dominant" is reliable. For the pixels with $0.9 \geq \alpha_g > 0.5$, the ground contribution is more dominant than the volume effect. In order to solve the equation, γ^v_{rand} is thus assumed to be negligible. Likewise, $\gamma^g_{d,\mathrm{rand}}$ should be ignored. This approach should be performed in each pixel and in each pair because pixels have different τ_g, τ_v, and μ, and α_g and α_v are different in every timespan

$$\text{if } 0.9 \geq \alpha_g > 0.5, \gamma^g_{d,\mathrm{rand}} = \frac{\gamma_{\mathrm{obs}} = \frac{1}{1+\mu}\exp\left(-\frac{\Delta T}{\tau_v}\right)}{\frac{\mu}{1+\mu}\exp\left(-\frac{\Delta T}{\tau_g}\right)} \tag{19}$$

$$\text{if } \alpha_g \leq 0.5, \gamma^v_{\mathrm{rand}} = \frac{\gamma_{\mathrm{obs}} = \frac{\mu}{1+\mu}\exp\left(-\frac{\Delta T}{\tau_g}\right)}{\frac{1}{1+\mu}\exp\left(-\frac{\Delta T}{\tau_v}\right)}. \tag{20}$$

C. Probability Map Generation

In previous sections, we presented the temporal decorrelation model and described the procedure for extracting the model parameters from multitemporal data. In this section, we outline the procedure used to estimate the changed area using model parameters. First, it is worth noting that the decorrelation effects are concentrated near the estimated envelope, as shown in Fig. 4. This implies that the decorrelation related to random-natural changes typically induce coherence that is concentrated at a certain level. Therefore, we can assume that $\gamma^g_{d,\mathrm{rand}}$ and γ^v_{rand} are nonuniformly distributed. A major event, such as volcanic ash, building collapse, or landslide, has a stronger contribution to the loss of coherence than the usual decorrelation related to natural phenomena. Accordingly, a major event usually results in lower $\gamma^g_{d,\mathrm{rand}}$ and γ^v_{rand} (brown bars in Fig. 7). A cumulative distribution function (CDF) of reference pairs (black lines in Fig. 7) offers statistical information about how strong and often the natural phenomena usually affect the observed coherence. Therefore, if these model parameters extracted from the event pair set are located at the tail of the probability density function (pdf), they can be assigned as "changed pixels," as indicated by the red rectangles in Fig. 7.

However, the pdf of the model parameters is undefined, the shape of the function is unknown, and the sample is also finite. Kernel density estimation (KDE) is an appropriate method for estimating unknown pdfs by smoothing the finite and discrete samples [36]. We applied KDE to estimate the pdf and build the continuous CDF of $\gamma^g_{d,\mathrm{rand}}$ and γ^v_{rand} of reference pairs.

We analyzed the statistics of model parameters according to dominant scattering because the numbers of available pairs are different. For example, when pixels are assigned as ground-dominant pixels ($\alpha_g > 0.9$), we can use interferometric pairs without consideration of perpendicular baseline. In our study, we created a histogram of $\gamma^g_{d,\mathrm{rand}}$ using 196 pairs (166 reference pairs and 30 event pairs) below 5000 m and estimated pdf using

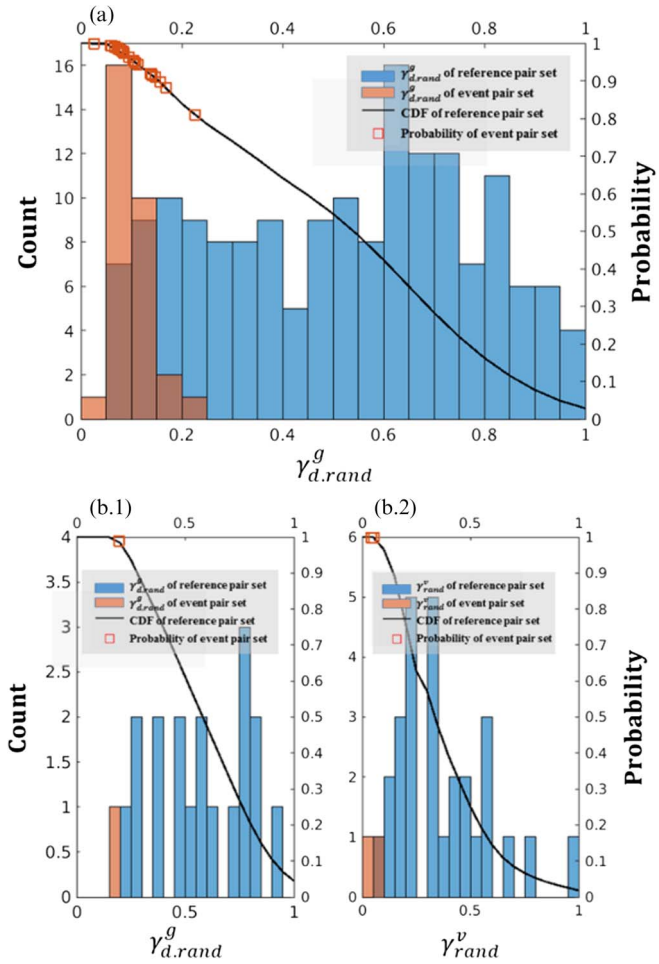

Fig. 7. (a) Histograms (blue bar) $\gamma^g_{d,\mathrm{rand}}$ in ground-dominant pixels and (b) $\gamma^g_{d,\mathrm{rand}}$ and γ^v_{rand} in ground-and-volume-coupled pixels. Brown histograms indicate corresponding value in event pair. Black lines are the estimated cumulative density functions using KDE, and red boxes are probability of event. This analysis was performed in the area denoted as A and D in Fig. 6.

the KDE method [Fig. 7(a)]. When the pixels are affected by the ground-volume-coupled effect ($\alpha_g \leq 0.9$), then estimation of the CDF has to be performed separately. Furthermore, when α_g is greater than 0.5, the $\gamma^g_{d,\mathrm{rand}}$ of reference pairs is used to estimate CDF, as shown in Fig. 7(b.1). Otherwise, γ^v_{rand} is used, as shown in Fig. 7(b.1). Consequently, two CDFs can exist in the coupled effect pixels. It is also worth noting that the number of interferometric pairs used in CDF is smaller than the number of ground-dominant pixels, owing to the limitation of the baseline (< 1000 m). In our case, we generated 47 reference pairs and 3 event pairs.

On the basis of the estimated cumulative density function from the reference pair set, the probability of a region having changed can be calculated using event pairs. Because two ALOS-PALSAR scenes were acquired after the volcanic eruption, it is obvious that they include the decorrelation caused by volcanic ash. Among all coherence maps generated using event pairs, only three interferometric pairs met the required baseline criterion, as shown in Fig. 8. One thing to keep in mind when interpreting the estimated probability is that the high probability results not only from volcanic ash but also from other factors including

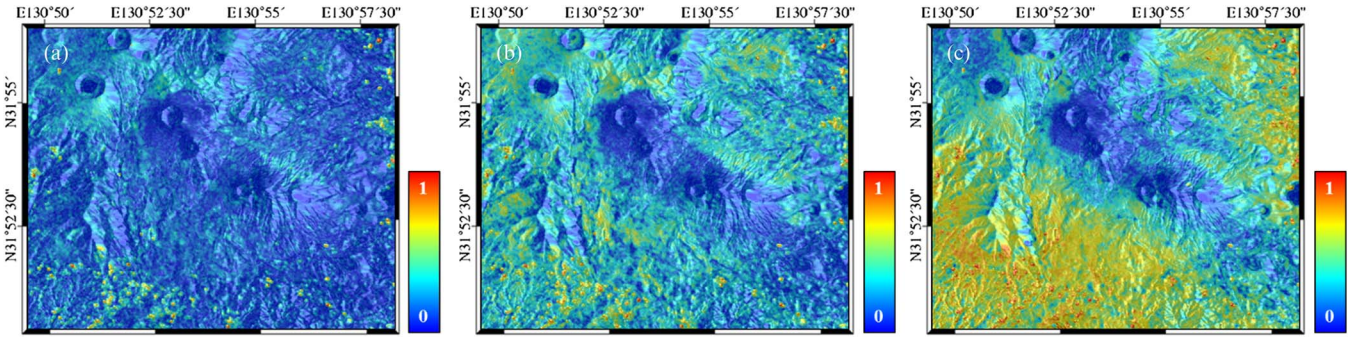

Fig. 8. Measured coherence maps generated over the periods (a) May 25, 2008–March 05, 2011; (b) December 03, 2010–March 05, 2011; and (c) January 18, 2011–March 05, 2011.

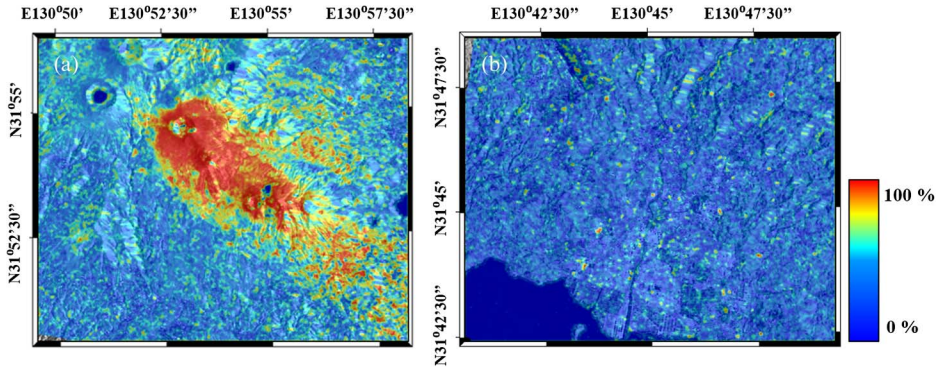

Fig. 9. Averaged probabilities of the event pairs of (a) Shinmoedake volcano and (b) Kirishima city.

heavy rain, strong wind, and other temporary changes. One simple and effective way to mitigate such short-lived events, compared to volcanic ash fall, is to average the probability of all pairs spanning the event. Averaging the probability plays an important role in enhancing the contribution of the interested event, which is volcanic ash. Fig. 9(a) shows the averaged probability map, on which the effect of volcanic ash is clearly observed near the southeast of the Shinmoedake volcano. Furthermore, significantly high probability values are sparsely distributed in Kirishima city [Fig. 9(b)]. This implies that Kirishima city was not affected by regional changes such as volcanic ash. Therefore, the result of Kirishima city clearly proves that the method proposed in this paper effectively discriminates changed regions from unchanged regions.

D. Mapping Volcanic Ash

To map volcanic ash, we compared the probability map with the *in situ* data and the contour lines [33], [37]. According to [33], the tephra plumes after eruption were dispersed by wind and deposited southeast of the Shinmoedake volcano. Furthermore, the thickness of volcanic ash deposits reached 4.5–25 cm in the proximal area. A comparison between the depth of the volcanic ash deposit and the probability map generated from our analysis showed a high probability over 2 cm, which corresponds to approximately 75%. For comparison with the contour lines, we averaged the probability values located between the contour line and the next level of the contour line. Accordingly, the values at the x-axis in Fig. 10(d) represent the small levels between two contour lines. The analysis with the area density shows a high correlation over 10 kg/m^2. This result does not mean that the calculated probability is directly related to the depth or the area density of the volcanic ash. In general, a thicker volcanic deposit might cause more phase alteration and thus strong temporal decorrelation. In addition, the probabilities at man-made structures are higher than other areas over 10 kg/m^2. The estimated probability is determined by the temporal behavior of coherence of the scatterers. If the scatterers are less affected by the natural phenomena, the historical coherence tends to be concentrated on a certain level. If a small amount of volcanic ash induces relatively low coherence, it can result in a high probability. This implies that, even though the same amount of volcanic ash was deposited, the sensitivity of change detection could be different. In the forest area, the random motion of volume and temporally uncorrelated dielectric changes are coupled in a complicated manner. This area is prone to decorrelation, and the coherence is concentrated in the low values. Thus, the decorrelation caused by a small amount of the volcanic ash may be hidden or unclear owing to the strong natural changes.

The analysis also shows that volcanic ash deposit below 10 kg/m^2 is uncorrelated with the probability. In order to mask out uncorrelated probability, we selected 75% as the threshold because 1σ (standard deviation) of uncorrelated probability reaches a maximum of 75%. Finally, we generated the change detection maps caused by the deposit of volcanic ash, as shown in Fig. 10(a).

IV. Conclusion

In this paper, we have proposed a temporal decorrelation model for coherence maps generated by multitemporal and single-polarimetric data to identify regions changed as a result

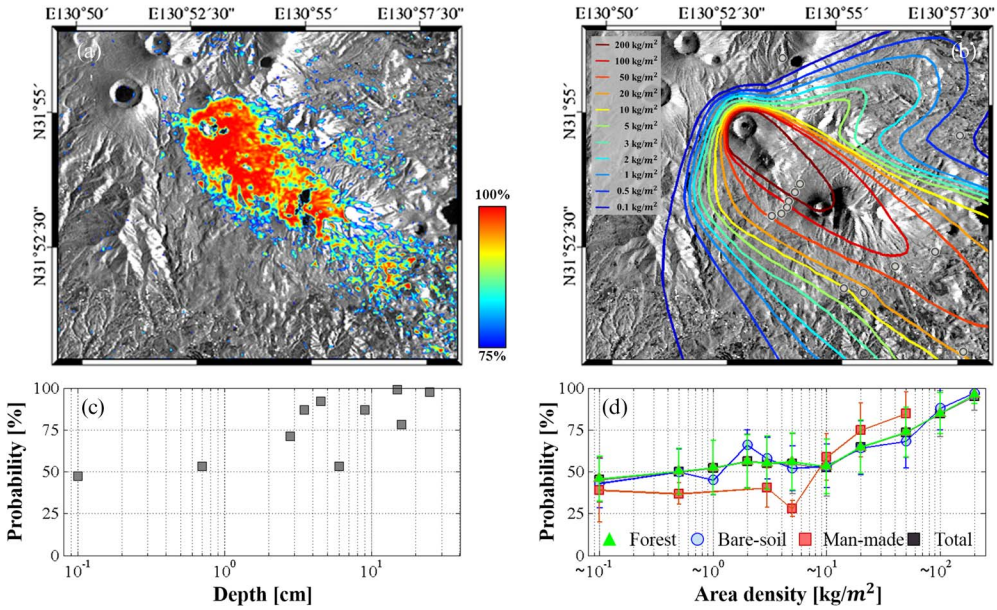

Fig. 10. (a) Estimated probability map over 75% and (b) the predicted distributed map of the volcanic ash and location of in-situ depth data. Comparison between estimated probability and (c) the depth of volcanic deposits and also between (d) area densities.

of the deposit of ash that follows volcanic eruptions. Our proposed temporal decorrelation model uses the ground-to-volume ratio, random motion of volume, temporally correlated dielectric changes in volume and ground, and temporally correlated changes in volume and ground. Because the number of variables involved in the temporal decorrelation exceeds the number of available equations, we have made several plausible assumptions. We have also showed that pixels with many scatterers have different temporal decorrelation behaviors depending on the temporally correlated dielectric changes and ground-to-volume ratio. In addition, the temporally uncorrelated dielectric changes and random motion of volume were also estimated based on the analysis of the portion of ground and volume coherence. To identify the coherence changes related to alterations in natural conditions, such as seasonal changes and meteorological phenomena, the KDE method was used to estimate the CDF for each pixel. Extreme changes caused by unexpected events such as deposition of volcanic ash, which yield abnormal values in the coherence map, were successfully extracted based on the CDF.

We have applied the proposed temporal decorrelation model to CCD and used it to estimate the physical parameters of the forest. The model carries out quantitative analysis involving physical parameters, which is not a common approach in CCD techniques. Consequently, it is very useful in areas with a variety of decorrelation sources. The special significance of our proposed method is that the model considers most of the decorrelation effects in order to be useful for many realistic and complex change detection applications. However, the several assumptions used to solve the main equation could still be controversial. Fortunately, recently developed fully polarimetric and interferometric SAR sensors onboard UAVSAR and ALOS-2 could reduce the effect of the assumptions or even render them more realistic. Further research using these sensors can show the usefulness of the temporal decorrelation model for the extraction of reliable physical parameters and generate more robust damage detection maps.

ACKNOWLEDGMENT

The ALOS PALSAR data used in this study were provided by the Japan Aerospace Exploration Agency (JAXA) through the Research Agreement for the Advanced Land Observing Satellite-1&2 (RA 3 and 4, PI No. 605 and 1407).

REFERENCES

[1] C. Yonezawa and S. Takeuchi, "Decorrelation of SAR data by urban damages caused by the 1995 Hyogoken-Nanbu earthquake," *Int. J. Remote Sens.*, vol. 22, no. 8, pp. 1585–1600, 2001.
[2] P. Gamba, F. Dell'acqua, and G. Trianni, "Rapid damage detection in the Bam area using multitemporal SAR and exploiting ancillary data," *IEEE Trans. Geosci. Remote Sens.*, vol. 45, no. 6, pp. 1582–1589, Jun. 2007.
[3] M. Matsuoka and F. Yamazaki, "Use of satellite SAR intensity imagery for detecting building areas damaged due to earthquakes," *Earthquake Spectra*, vol. 20, no. 3, pp. 975–994, 2004.
[4] J. B. Collins and C. E. Woodcock, "An assessment of several linear change detection techniques for mapping forest mortality using multitemporal Landsat TM data," *Remote Sens. Environ.*, vol. 56, no. 1, pp. 66–77, Apr. 1996.
[5] A. Singh, "Review article digital change detection techniques using remotely-sensed data," *Int. J. Remote Sens.*, vol. 10, no. 6, pp. 989–1003, 1989.
[6] D. Lu, P. Mausel, E. Brondizio, and E. Moran, "Change detection techniques," *Int. J. Remote Sens.*, vol. 25, no. 12, pp. 2365–2407, 2004.
[7] M. Preiss, D. A. Gray, and N. J. Stacy, "Detecting scene changes using synthetic aperture radar interferometry," *IEEE Trans. Geosci. Remote Sens.*, vol. 44, no. 8, pp. 2041–2054, Aug. 2006.
[8] E. J. M. Rignot and J. J. van Zyl, "Change detection techniques for ERS-1 SAR data," *IEEE Trans. Geosci. Remote Sens.*, vol. 31, no. 4, pp. 896–906, Jul. 1993.
[9] R. Dekker, "Speckle filtering in satellite SAR change detection imagery," *Int. J. Remote Sens.*, vol. 19, no. 6, pp. 1133–1146, 1998.
[10] M. Gong, Z. Zhou, and J. Ma, "Change detection in synthetic aperture radar images based on image fusion and fuzzy clustering," *IEEE Trans. Image Process.*, vol. 21, no. 4, pp. 2141–2151, Apr. 2012.
[11] G. Nico, M. Pappalepore, G. Pasquariello, A. Refice, and S. Samarelli, "Comparison of SAR amplitude vs. coherence flood detection methods—A GIS application," *Int. J. Remote Sens.*, vol. 21, no. 8, pp. 1619–1631, 2000.
[12] F. Bovolo and L. Bruzzone, "A detail-preserving scale-driven approach to change detection in multitemporal SAR images," *IEEE Trans. Geosci. Remote Sens.*, vol. 43, no. 12, pp. 2963–2972, Dec. 2005.

[13] R. G. White and C. J. Oliver, "Change detection in SAR imagery," in *Proc. IEEE Int. Radar Conf.*, Arlington, TX, USA, 1990, pp. 217–222.
[14] Y. Bazi, L. Bruzzone, and F. Melgani, "An unsupervised approach based on the generalized Gaussian model to automatic change detection in multitemporal SAR images," *IEEE Trans. Geosci. Remote Sens.*, vol. 43, no. 4, pp. 874–887, Apr. 2005.
[15] G. Moser and S. B. Serpico, "Generalized minimum-error thresholding for unsupervised change detection from SAR amplitude imagery," *IEEE Trans. Geosci. Remote Sens.*, vol. 44, no. 10, pp. 2972–2982, Oct. 2006.
[16] W. M. F. Grey, A. J. Luckman, and D. Holland, "Mapping urban change in the U.K. using satellite radar interferometry," *Remote Sens. Environ.*, vol. 87, no. 1, pp. 16–22, Sep. 2003.
[17] A. Bouaraba, A. Younsi, A. Belhadj Aissa, M. Acheroy, N. Milisavljevic, and D. Closson, "Robust techniques for coherent change detection using COSMO-SkyMed SAR images," *Progr. Electromagn. Res.*, vol. 22, pp. 219–232, 2012.
[18] D. Geudtner, R. Winter, and P. W. Vachon, "Flood monitoring using ERS-1 SAR interferometry coherence maps," in *Proc. IEEE IGARSS*, Lincoln, NE, USA, 1996, pp. 966–968.
[19] F. Rocca, "Modeling interferograms stacks," *IEEE Trans. Geosci. Remote Sens.*, vol. 45, no. 10, pp. 3289–3299, Oct. 2007.
[20] M. Lavalle and S. Hensley, "Extraction of structural and dynamic properties of forests from polarimetric-interferometric SAR data affected by temporal decorrelation," *IEEE Trans. Geosci. Remote Sens.*, vol. 53, no. 9, pp. 4752–4767, Sep. 2015.
[21] M. Lavalle, M. Simard, and S. Hensley, "A temporal decorrelation model for polarimetric radar interferometers," *IEEE Trans. Geosci. Remote Sens.*, vol. 50, no. 7, pp. 2880–2888, Jul. 2012.
[22] H. Zebker and J. Villasenor, "Decorrelation in interferometric radar echoes," *IEEE Trans. Geosci. Remote Sens.*, vol. 30, no. 5, pp. 950–959, Sep. 1992.
[23] M. Wei and D. T. Sandwell, "Decorrelation of L-band and C-band interferometry over vegetated areas in California," *IEEE Trans. Geosci. Remote Sens.*, vol. 48, no. 7, pp. 2942–2952, Jul. 2010.
[24] R. Bamler and D. Just, "Phase statistics and decorrelation in SAR interferograms," *System*, vol. 1, p. E2, 1995.
[25] B. Sun, J. Chen, C.-S. Li, and Y.-Q. Zhou, "FA-SCANSAR: Full aperture scanning pulse by pulse for the nearspace slow-moving platform borne SAR," *Progr. Electromagn. Res. B*, vol. 25, pp. 23–37, 2010.
[26] J. Askne, P. B. Dammert, L. M. Ulander, and G. Smith, "C-band repeat-pass interferometric SAR observations of the forest," *IEEE Trans. Geosci. Remote Sens.*, vol. 35, no. 1, pp. 25–35, Jan. 1997.
[27] S. R. Cloude and K. P. Papathanassiou, "Polarimetric SAR interferometry," *IEEE Trans. Geosci. Remote Sens.*, vol. 30, no. 5, pp. 1551–1565, Sep. 1998.
[28] K. P. Papathanassiou and S. R. Cloude, "Single-baseline polarimetric SAR interferometry," *IEEE Trans. Geosci. Remote Sens.*, vol. 39, no. 11, pp. 2352–2363, Nov. 2001.
[29] S. Cloude and K. Papathanassiou, "Three-stage inversion process for polarimetric SAR interferometry," *Proc. Inst. Elect. Eng.—Radar, Sonar Navigat.*, vol. 150, no. 3, pp. 125–134, Jun. 2003.
[30] O. Stebler, E. Meier, and D. Nüesch, "Multi-baseline polarimetric SAR interferometry—First experimental spaceborne and airborne results," *ISPRS J. Photogramm. Remote Sens.*, vol. 56, no. 3, pp. 149–166, 2002.
[31] P. Rosen *et al.*, "Synthetic aperture radar interferometry," *Proc. IEEE*, vol. 88, no. 3, pp. 333–382, Mar. 2000.
[32] F. Lombardini and H. Griffiths, "Effect of temporal decorrelation on 3D SAR imaging using multiple pass beamforming," in *Proc. IEE/EUREL Meet. Radar Sonar Signal Process.*, Peebles, U.K., Jul. 1998, pp. 1–4.
[33] Y. Miyabuchi, D. Hanada, H. Niimi, and T. Kobayashi, "Stratigraphy, grain-size and component characteristics of the 2011 Shinmoedake eruption deposits, Kirishima Volcano, Japan," *J. Volcanol. Geothermal Res.*, vol. 258, pp. 31–46, 2013.
[34] M. Takahashi *et al.*, "JAXA high resolution land-use and land-cover map of Japan," in *Proc. IEEE IGARSS*, Melbourne, Vic., Australia, 2013, pp. 2384–2387.
[35] M. Shimada, O. Isoguchi, T. Tadono, and K. Isono, "PALSAR radiometric and geometric calibration," *IEEE Trans. Geosci. Remote Sens.*, vol. 47, no. 12, pp. 3915–3932, Dec. 2009.
[36] A. Bowman and A. Azzalini, *Applied Smoothing Techniques for Data Analysis*. New York, NY, USA: Oxford Univ. Press, 1997.
[37] "Isomass contours that describes ash accumulation from Kirishimayama-Shinmoedake eruption between 26 and 27 January, 2011," Nat. Inst. Adv. Ind. Sci. Technol. (AIST), Tokyo, Japan, 2011. [Online]. Available: http://www.aist.go.jp/aist_j/press_release/pr2011/pr20110201_2/pr20110201_2.html

Jungkyo Jung received the B.S. and M.S. degrees in earth and environmental sciences from Seoul National University, Seoul, South Korea, in 2011 and 2013, respectively, where he is currently working toward the Ph.D. degree in satellite geophysics.

His interests in research include synthetic aperture radar interferometry, coherence change detection, time-series interferometry, and volcanology.

Duk-jin Kim (M'05–SM'16) received the B.Sc. degree in earth system science and the M.Sc. and Ph.D. degrees in radar remote sensing and geophysics from Seoul National University, Seoul, South Korea, in 1999, 2001, and 2005, respectively.

From October 2005 to July 2007, he was a Postdoctoral Researcher with the University of Manitoba, Winnipeg, MB, Canada, and with the University of Michigan, Ann Arbor, MI, USA. From July 2007 to August 2008, he was a Senior Researcher with the Remote Sensing Division, Korea Aerospace Research Institute, Daejeon, South Korea. He is currently an Associate Professor with the School of Earth and Environmental Sciences, Seoul National University. During his sabbatical leave from August 2014 to July 2015, he was a Visiting Scholar with the Radar Science and Engineering Section, Jet Propulsion Laboratory, California Institute of Technology, Pasadena, CA, USA. His research interests include coastal environment and disaster monitoring using spaceborne and airborne synthetic aperture radar (SAR) systems, as well as ocean/sea ice parameter extractions using along-track interferometric and polarimetric SAR data.

Marco Lavalle received the Master's degree in telecommunication engineering from the University of Rome Tor Vergata, Rome, Italy, in 2006 and the Ph.D. degree in electrical engineering from the University of Rennes 1, Rennes, France, and from the University of Rome Tor Vergata in December 2009.

From 2006 to 2008, he was a Visiting Researcher with the ESRIN facility of the European Space Agency, where he developed algorithms for polarimetric radar calibration and forest parameter retrieval. From January 2010 to December 2011, he was a NASA Postdoctoral Fellow with the Jet Propulsion Laboratory, California Institute of Technology, Pasadena, CA, USA. Since January 2012, he has been a Scientist with the Radar Science and Engineering Section, Jet Propulsion Laboratory, California Institute of Technology. He is currently a Principal Investigator for the NASA Terrestrial Ecology Program and a member of the NASADEM and NISAR Project Science teams. His research interests include electromagnetic propagation and scattering theory, physical modeling of polarimetric and interferometric radar signals, characterization of interferometric temporal decorrelation, inverse theory, and biophysical parameter modeling and estimation.

Dr. Lavalle received the Student Prize Paper Award at the EUSAR 2008 Conference, Friedrichshafen, Germany.

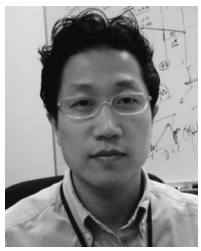

Sang-Ho Yun received the M.S. degree in electrical engineering and the Ph.D. degree in geophysics from Stanford University, Stanford, CA, USA.

He is currently a Geophysicist and Radar Engineer with the Radar Science and Engineering Section, NASA Jet Propulsion Laboratory (JPL), California Institute of Technology, Pasadena, CA. He is a Principal Investigator for two NASA projects to develop: 1) building damage detection algorithms using SAR and 2) modeling tools for volcanic deformation using seismicity and geodetic observations. Prior to joining JPL, he was a Postdoctoral Fellow with the U.S. Geological Survey, Menlo Park, CA.

Dr. Yun was a recipient of the 2014 NASA Honor Award for Exceptional Early Career Achievements in the Development of Post-disaster Assessments using Spaceborne Synthetic Aperture Radar.